Flexural-mode solid-state thermoacoustics

Haitian Hao [a,b], Carlo Scalo [a], Fabio Semperlotti [a,b,*]

[a] *School of Mechanical Engineering, Purdue University, West Lafayette, IN 47907, USA*
[b] *Ray W. Herrick Laboratories, 177 South Russell Street, West Lafayette, IN 47907, USA*

ARTICLE INFO

ABSTRACT

Recent studies have indicated that axial waves traveling in a one dimensional solid rod can give rise to a thermoacoustically unstable response when in presence of an externally applied spatial temperature gradient. Similar to fluid-based thermoacoustics, both standing and traveling axial thermoacoustic waves can exist in solids. Elastic waves in solids are polarized, hence it is reasonable to hypothesize that thermoacoustic instabilities can affect also shear-type waves, such as flexural waves. This study extends previous research on axial-mode solid-state thermoacoustics to flexural-mode solid-state thermoacoustics (F-SSTAs). More specifically, it is shown how flexural waves can grow unbounded when traveling in a bilayer beam subject to a spatial thermal gradient. A theoretical framework is developed to analyze the dynamics of the system and to establish the criterion controlling the onset of flexural thermoacoustic instability. Numerical calculations conducted in both the frequency and the time domains show the occurrence of two main effects due to the presence of thermal coupling: (1) the dynamic amplification of the flexural motion, and (2) the time-varying location of the neutral axis. An experimental investigation is also conducted in order to corroborate the existence of this thermal-to-mechanical energy conversion mechanism associated with flexural waves.

© 2020 Elsevier Ltd. All rights reserved.

1. Introduction

Thermoacoustic (TA) instability is a well-established phenomenon commonly occurring in fluids. The theoretical foundation of TA instability was laid by Rott in 1969 [1]. The energy conversion mechanism at the basis of TA oscillations [2] inspired the design of thermoacoustic engines (TAEs) [3–6] and refrigerators (TARs) [7,8]. A classical example of TAE is the Rijke's tube [9] which amplifies acoustic waves due to the heat transfer between a heated metal mesh and the convection-induced upward flowing air. Although initial TAE designs [3,4] require very high temperature to trigger the thermoacoustic instability, efforts have been made to lower the onset temperature for low-grade heat recovery with various approaches such as, for example, phase adjustment in sound field using by-pass tube [10] or compliance and resistance section [11], and gas-liquid phase change in thermofluidic oscillations [12–14]. Linear and nonlinear Navier-Stokes simulations of both standing- and traveling-wave TAEs have been conducted to understand the energy conversion process and to predict the engine performance [15–18]. For practical applications, energy harvesting elements can be integrated with TAEs to accomplish an additional mechanical-to-electrical energy conversion process [19–22].

Only recently, the theory of TA oscillations in solids, namely solid-state thermoacoustics (SSTAs), was established [23,24]. These studies showed, by theoretical and numerical means, the existence of self-sustained longitudinal TA oscillations in

---

* Corresponding author at: School of Mechanical Engineering, Purdue University, West Lafayette, IN 47907, USA.
  E-mail addresses: haoh@purdue.edu (H. Hao), scalo@purdue.edu (C. Scalo), fsemperl@purdue.edu (F. Semperlotti).

solids, hence providing a direct counterpart to the well-known thermoacoustic response of fluids. Both standing and travel-ing axial-mode wave configurations were explored. The latter configuration showing a higher efficiency of the energy con-version mechanism [25]; an observation consistent with fluid-based TA systems. Later, parametric analyses based on analytical approaches [26] provided optimal design guidelines for both standing- and traveling-wave solid-state thermoa-coustic engines.

Unlike in fluids, waves in solids are polarized which means that, beyond the primary (also known as longitudinal or axial) waves, two shear-type waves are also admissible states of motion. The shear-type waves, which are not present in fluids, produce particle motion in a direction perpendicular to the direction of propagation. In finite elastic waveguides, shear waves give rise to flexural type of motion. The goal of the present study is to establish the theoretical framework of flexural solid-state thermoacoustics, an extension to previous research focusing on axial-mode solid-state thermoacoustics, and to discuss the existence of unstable flexural thermoacoustic waves in certain types of solid-state devices. More specifically, this study focuses on a bilayer slender beam subject to two types of spatial thermal gradients. The *Type I* gradient is linear and, although less practical for an experimental implementation, it allows a fully analytical treatment of the dynamical problem hence facilitating the detailed understanding and the physical interpretation of the phenomenon. In the *Type II* gradient, the inward heat flux is a sign function of the transverse displacement. This type of gradient is instead more amenable to an experimental implementation, but it does not allow an analytical solution of the governing equations. Theoretical analyses of the flexural motion of the bilayer beam under these two types of heating reveal the criterion to determine the occurrence of flexural instability. Also, the dynamics of the neutral axis location and the mechanism behind the self-amplifying flexural solid-state thermoacoustic (F-SSTA) oscillations will be explored in detail. The theoretical model developed in this work to determine the onset and the strength of the instability is based on the linearized Euler-Bernoulli theory. It follows that the nonlinear effects in thermoacoustic systems (e.g. acoustic streaming) are not captured by the proposed model. Note that these effects are well-understood in classical theory of thermoacoustics and do not limit the generality of the results pre-sented in this manuscript. Specifically, the acoustic streaming phenomenon is not expected in solid systems.

The results of an experimental investigation of the thermoacoustic response of a bilayer beam will also be presented. Although a fully self-sustained flexural motion was not observed due to the limited heating and cooling capacity, a visibly reduced effective damping rate was achieved, demonstrating that the thermal-to-mechanical energy conversion process does exist in an F-SSTA system.

After discussing the F-SSTAs from a theoretical, numerical, and experimental perspective, we will contrast it with the con-cept of thermal flutter previously observed in space applications [27,28].

2. Problem statement

Consider the small amplitude dynamic response of a slender beam. Under Euler-Bernoulli assumptions, the force balance of an infinitesimal beam element of an arbitrary cross section in the transverse direction is given by:

$$\rho \mathscr{A} \frac{\partial^2 v}{\partial t^2} = \frac{\partial \mathscr{Q}}{\partial x} \tag{1}$$

where $\mathscr{A}$ is the total area of the beam cross section, v is the transverse displacement, $\rho = \left(\int_{\mathscr{A}} \varrho d\mathscr{A}\right)/\mathscr{A}$ is the effective den-sity, ϱ is the density distribution over the across section, $\mathscr{Q} = \partial \mathscr{M}/\partial x$ is the shear force, $\mathscr{M} = \int_{\mathscr{A}} \sigma y d\mathscr{A}$ is the bending moment and σ is the axial stress defined as:

$$\sigma = E(\varepsilon - \alpha T) = E\left(-y\frac{\partial^2 v}{\partial x^2} - \alpha T\right) \tag{2}$$

where E and α are the Young's modulus and the linear thermal expansion coefficient, $\varepsilon = -y(\partial^2 v)/(\partial x^2)$ is the axial strain and T is the temperature fluctuation. y is the transverse coordinate defined from the neutral axis of the cross section.

In this study, we consider the case of a beam having a rectangular cross section formed by two adjoined layers of different material having the same width b and height $h/2$ (Fig. 1(b)). We assume an ideal interface between the two layers hence discard the possibility of relative slip.

The flexural motion of the beam is governed by:

$$\rho h \frac{\partial^2 v}{\partial t^2} = \frac{\partial^2 m}{\partial x^2} \tag{3}$$

where the effective density $\rho = (\rho_1 + \rho_2)/2$, m is the moment per unit width expressed as:

$$m = \int_{-h_1}^{h_0} \sigma_1 y dy + \int_{h_0}^{h_2} \sigma_2 y dy \tag{4}$$

where σ is the axial stress defined in Eqn. (2). For the ith layer (with $i = 1, 2$), the axial stress is given by:
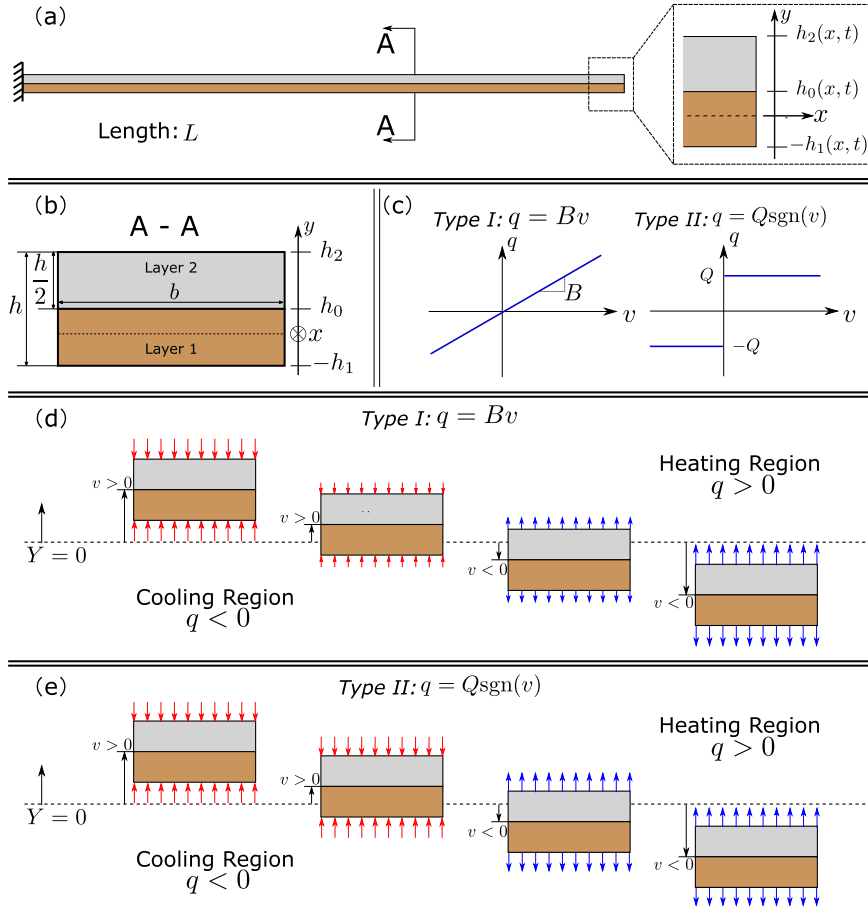
Fig. 1. (a) and (b) Basic notation and local coordinate frame for the bilayer beam. The cross section is made out of two rectangular layers having identical width b and height $h/2$. The dashed line indicates the position of the neutral axis of the cross section, where the local coordinate y is defined. The location of the interface, as well as the bottom and top surfaces of the cross section are at h_0, $-h_1$, and h_2 in this local frame. Under thermoacoustic coupling, the neutral axis location is not necessarily time-invariant, implying that h_0, h_1, and h_2 can change with time. (c) Top and bottom surfaces of the cross section experience heat flux (positive if inward). Two types of thermal loads are investigated, namely $q = Bv$ and $q = Q\mathrm{sgn}(v)$. (d) and (e) The beam moving from heating region to cooling region under (d) Type I: $q = Bv$ and (e) Type II : $q = Q\mathrm{sgn}(v)$ thermal loads. The red and blue arrows indicate surface heating and cooling, respectively. The length of the arrows indicate the strength of q. Note that in the second and the third configuration in (d), the arrows are shorter due to a smaller v. The heating ($q > 0$) and cooling ($q < 0$) regions are divided by the spatial transverse coordinate $Y = 0$. The equilibrium position of the flexural vibration of the beam, $v = 0$, is coincident with $Y = 0$ in the absolute reference frame. Euler–Bernoulli theory assumes homogeneous displacement v over the cross section, so once the geometric center of the beam is positively displaced (left two configurations), the upper and bottom surfaces experience inward heating, and vice versa for the two configurations on the right.

$$\sigma_i = E_i\left(-y\frac{\partial^2 v}{\partial x^2} - \alpha_i T_i\right), \qquad (i = 1, 2) \tag{5}$$

Note again that y is a local coordinate defined at the neutral axis (Fig. 1(a) and (b)) which, as clarified in the following, can change its position due to the effect of the thermoelastic coupling. In Eqn. (5), the first term on the right hand side represents the mechanical stress while the second term represents the thermoelastic stress. h_0 in Eqn. (4) indicates the location of the neutral axis on the local coordinate system y (Fig. 1(a) and (b)). The magnitude of h_0 denotes the distance between the neutral axis and the interface between the two layers. h_1 and h_2 are related to h_0 by:

$$h_1 + h_0 = \frac{h}{2} \tag{6}$$

$$h_2 - h_0 = \frac{h}{2} \tag{7}$$

The neutral axis location h_0 is determined by imposing a vanishing total axial force:

$$\int_{-h_1}^{h_0} \sigma_1 dy + \int_{h_0}^{h_2} \sigma_2 dy = 0 \tag{8}$$

which yields:

$$h_0 = h_e - \frac{AI_T}{(h/2)\,v_{xx}(n+1)} \tag{9}$$

where $h_e = h(n-1)/4(n+1)$ denotes the neutral axis location in a purely elastic bilayer beam with no thermoelastic coupling, $n = E_1/E_2$, and v_{xx} is a compact notation for $\partial^2 v/\partial x^2$. The second term in Eqn. (9) shows the effect of thermoelastic coupling. AI_T is given by:

$$AI_T = n\alpha_1 \int_{-h_1}^{h_0} T_1 dy + \alpha_2 \int_{h_0}^{h_2} T_2 dy \tag{10}$$

Eq. (9) shows that, unlike its elastic counterpart, the location of the neutral axis of a beam in presence of thermoelastic coupling depends on the temperature fluctuations in the cross section. Consequently, the location of the neutral axis is a function of both time t and spatial x coordinates.

The fluctuating temperature field in the 2D beam is governed by:

$$\rho_i c_{\varepsilon_i} \frac{\partial T_i}{\partial t} + E_i \alpha_i T_0 \frac{\partial \varepsilon}{\partial t} = k_i \left(\frac{\partial^2 T_i}{\partial x^2} + \frac{\partial^2 T_i}{\partial y^2} \right) \tag{11}$$

where k_i and c_{ε_i} are thermal conductivity and specific heat at constant strain. The mean temperature T_0 is assumed as the ambient temperature set at 293.15 K. The second term on the left-hand side is the heat source induced by the thermoelastic coupling, as a result of the local heat flux caused by the stress inhomogeneity [29]. According to thermodynamic laws, this local heat flux leads to an entropy increase, reflected in a (very slow) rise of the mean temperature T_0. However, in this study, only the fluctuating temperature is considered and the slow variation of T_0 is neglected. From a dynamic perspective, this irreversible process dissipates kinetic energy and induces a slow decay of the response that is well known as thermoelastic damping (TED) [30].

Note that although coupling the thermal and elastic fields induces the existence of TED, this quantity differs from the structural damping which is an intrinsically dissipative mechanism in solids. Damping in structures is the result of multiple mechanisms of energy dissipation. The most significant for the system under investigation are:

1. *Structural damping:* Structural damping is a macroscopic manifestation of non-conservative dissipative mechanisms occurring at the micro (and smaller) scales such as, for example, internal friction due to structural impurity and inhomogeneity, or motion of dislocations and defects [31]. These mechanisms convert irreversibly mechanical energy into heat, and manifest themselves at the macroscale as an attenuating effect on the vibratory response of the system. In practical systems, the heat produced by this mechanism either leaves the structures by radiation, by conduction through the boundaries, or it raises the mean temperature of the structure. Independently of the mechanisms taking place at the microscale, the heat produced via the structural damping has a negligible effect on the F-SSTA mechanism and can be neglected.

2. *Thermoelastic damping (TED):* TED is a result of thermoelastic coupling. It appears in ideal continuous solids, as well as real materials, due to the irreversible entropy increase caused by stress inhomogeneity. The heat produced by TED also leads to a very slow rise of the mean temperature of the structure, which is neglected compared to the fast thermoacoustic dynamics in solids.

3. *Fluid-structure interaction (FSI) induced damping:* This aspect includes sound emission and aerodynamic damping, which converts part of the mechanical energy of the structure into motion of the fluid in contact with the structure. Sound emission takes place when the structure vibrates beyond a certain frequency, known as the cut-on frequency (or equivalence, the cut-off frequency, or the critical coupling frequency). The aerodynamic damping is strictly dependent on the amplitude of the oscillatory motion and increases with it. Both these effects result in an attenuation of the vibratory motion.

We can further clarify some differences between structural damping and TED. Although they both produce a conversion of mechanical energy into heat loss, TED is an example of "*extrinsic damping sources and result from the bulk response of a material*", as stated in [31]. Structural damping, sometime referred to as defect damping, "*is an intrinsic damping source and results from internal friction due to the cyclic movement of defects in the material*" [31]. In the theoretical analysis of this paper, we only capture the TED. The decision to neglect the FSI-induced damping and the structural damping follows from these considerations: 1) the sound emission effect is absent due to the low operating frequency, below the cut-on frequency of the corresponding mode, 2) the aerodynamic damping is negligible due to the small oscillation amplitude assumption, 3) the structural damping is also neglected since its effect is extensively studied (e.g. [31]) and well understood. Most importantly, neglecting structural damping simplifies the theoretical derivations and analyses, allowing us to gain deeper insights

in the underlying mechanisms of the two main effects under thermoacoustic coupling: TED and F-SSTA amplification. Still, one can easily account for the structural damping in numerical simulations. Its effect is also observed in the experiments. A more detailed discussion can be found in Section 5.

The thermoacoustic response of a cantilever bilayer beam subject to two different types of surface heating will be considered (Fig. 1(c)). *Type I* is $q = Bv$, where q is the inward heat flux on the top ($y = h_2$) and bottom ($y = -h_1$) surfaces, and B is a constant. This type of heating represents a linear thermal gradient anchored in space (with a transverse coordinate Y in spatial frame, see Fig. 1(d)). We assume that the equilibrium position of the beam, $v = 0$, is aligned with the $Y = 0$ location in the absolute spatial frame. As a result, the beam experiences a linearly varying rate of heating (cooling) as it vibrates in the positive (negative) Y domain. *Type II* is $q = Q\text{sgn}(v)$, where Q is a constant value and sgn() is the sign function. This type of surface heating represents an abrupt change of heat flux in space as the beam moves through the upper half plane towards the lower half plane. Note that the Euler-Bernoulli theory assumes that the flexural displacement v is homogeneous across the cross section, while the stress and the temperature in presence of thermoelastic coupling are not. It follows that, when taking these two types of heating into consideration, once the geometric center of the cross section is positively (negatively) displaced, i.e. $v > 0$ ($v < 0$), the whole cross section experiences surface heating (cooling), as shown in Fig. 1(d) and (e). The analysis for *Type I* is based on a modal approach which allows developing useful analytical expressions to understand the physical mechanisms governing the coupled dynamic response of the system. *Type II* is analyzed instead by using time-domain numerical integration. It confirms the existence of the self-amplifying mechanism due to F-SSTAs. The time evolution of neutral axis location h_0 associated with the flexural instability is observed and analyzed.

Under the two types of thermal loads, we adopted different assumptions for (1) the neutral axis location, (2) the interfacial thermal resistance, and (3) the thermoelastic damping. The basis for these assumptions will be articulated in details in the following. The assumptions corresponding to the two thermal loads are shown in Fig. 2.

3. *Type I: q = Bv* heating

This thermal load case is selected to obtain analytical solutions capable of describing the dynamics of the F-SSTA bilayer beam while revealing the role of the design parameters on both the dynamic response and the occurrence of the instability. We will first assume a time-invariant neutral axis location h_0 in Section 3.1, which allows a relatively compact and quantitatively accurate estimate of the growth rate and natural frequency. Then in Section 3.2, we will remove the constant h_0 assumption and explore the dynamics of the neutral axis under thermoelastic coupling. The latter assumption, despite its modeling and computational complexity, provides a more accurate representation of the underlying physics.
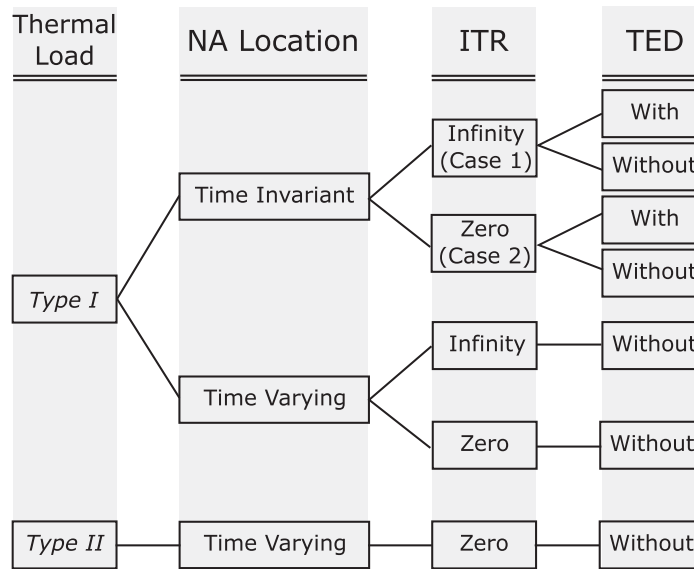
NA: Neutral Axis **ITR**: Interfacial Thermal Resistance **TED**: Thermoelastic Damping

Fig. 2. Assumptions adopted for the analyses in Sections 3 and 4, corresponding to the two thermal loads for (1) the neutral axis (NA) location, (2) the interfacial thermal resistance (ITR), and (3) the thermoelastic damping (TED). Specifically, the cases with infinite and zero interfacial thermal resistance assumptions are referred to Case 1 and Case 2 in Sections 3 and 4.

3.1. Time-invariant neutral axis location (Constant h_0)

In this section, we assume $h_0 = h_e$ where h_e is a constant value denoting the location of the neutral axis in a bilayer beam with no thermoelastic coupling. This is a common assumption in most studies on thermal induced vibrations [32,27,33,34] and implies that the second term in the right-hand side of Eqn. (9) is neglected.

Under this assumption, Eq. (3) becomes:

$$\rho h \frac{\partial^2 v}{\partial t^2} + D \frac{\partial^4 v}{\partial x^4} + \frac{\partial^2 m_T}{\partial x^2} = 0 \tag{12}$$

where D is flexural rigidity expressed as:

$$D = \frac{1}{3} E_2 \left[n \left(h_0^3 - \left(h_0 - \frac{h}{2} \right)^3 \right) + \left(h_0 + \frac{h}{2} \right)^3 - h_0^3 \right] \tag{13}$$

The thermal moment per unit width m_T is expressed as:

$$m_T = E_2 \left(n\alpha_1 \int_{-h_1}^{h_0} yT dy + \alpha_2 \int_{h_0}^{h_2} yT dy \right) \tag{14}$$

The assumed $q = Bv$ heating implies the following boundary conditions for the temperature on the free surfaces:

$$-k_2 \frac{\partial T_2}{\partial y} \bigg|_{y=h_2} = -Bv \tag{15}$$

$$-k_1 \frac{\partial T_1}{\partial y} \bigg|_{y=-h_1} = Bv \tag{16}$$

Assume the variables are harmonic in time so that $() = \hat{()} e^{i\lambda t}$, where the complex frequency $\lambda = \omega - i\beta$, i is the imaginary unit, β is the growth/decay rate, and ω is the angular frequency. $\hat{()}$ denotes quantities in modal space. By neglecting the heat conduction in x (since the heat flows mainly in the transverse direction), Eqn. (11) becomes:

$$(i\lambda)\hat{T}_i = \frac{k_i}{\rho_i c_{\varepsilon_i}} \left(\frac{\partial^2 \hat{T}_i}{\partial y^2} \right) + \gamma_i T_0 y (i\lambda) \frac{\partial^2 \hat{v}}{\partial x^2} \tag{17}$$

where $\gamma_i = E_i \alpha_i / (\rho_i c_{\varepsilon_i})$ is the Grüneisen parameter. Note that neglecting the axial diffusion term is a very common simplification used in thermoacoustics [1] because the axial derivative is on the order of $1/\lambda_w$, much smaller than the transverse derivative which is on the order of $1/\delta_k$. λ_w and δ_k are the wavelength and the thermal penetration depth, respectively. This assumption is due to the large difference in scale between $1/\lambda_w$ and $1/\delta_k$, so it is reasonable for solids as well.

Eq. (17) can be solved for $\hat{T}$, yielding:

$$\hat{T}_i = C \cos \left(\frac{\sqrt{-2i}}{\delta_{k_i}} y \right) + S \sin \left(\frac{\sqrt{-2i}}{\delta_{k_i}} y \right) + \gamma_i T_0 y \frac{\partial^2 \hat{v}}{\partial x^2} \tag{18}$$

where C and S are coefficients to be determined based on the boundary conditions. Converting Eqn. (14) into modal space and substituting $\hat{T}_i$ from Eqn. (18) yields:

$$\hat{m}_T = c_A \hat{v} + c_E \hat{v}_{xx} \tag{19}$$

where c_A and c_E are complex coefficients and their real and imaginary parts are determined by the constants C and S.

In the following, the two cases of different interfacial thermal conditions: Case 1 (infinite thermal resistance) and Case 2 (zero thermal resistance) are analyzed separately. Note that a realistic interface has finite thermal resistance, so the two cases represent the upper and lower bounds of a realistic case.

Case 1: Infinite interfacial thermal resistance

Assuming that the thermal resistance at the interface is infinitely large, no heat flux is allowed at the interface, therefore:

$$\frac{\partial T_2}{\partial y} \bigg|_{y=h_0} = \frac{\partial T_1}{\partial y} \bigg|_{y=h_0} = 0 \tag{20}$$

By applying the counterpart of Eqns. (15), (16) and (20) in modal space, the temperature field in each layer is found as:

$$\hat{T}_i = -\frac{B}{k_i} \frac{\delta_{k_i}}{\sqrt{-2i}} \frac{\cos \left[\frac{\sqrt{-2i}}{\delta_{k_i}} (h_0 - y) \right]}{\sin \left[\frac{\sqrt{-2i}}{\delta_{k_i}} \frac{h}{2} \right]} \hat{v} + \gamma_i T_0 \left\{ y - \frac{\delta_{k_i}}{\sqrt{-2i}} \frac{\sin \left[\frac{\sqrt{-2i}}{\delta_{k_i}} \left(y - h_0 \pm \frac{h}{4} \right) \right]}{\cos \left[\frac{\sqrt{-2i}}{\delta_{k_i}} \frac{h}{4} \right]} \right\} \hat{v}_{xx} \tag{21}$$

where the $\pm$ sign is replaced by a plus sign for layer 1 ($i = 1$) and a minus sign for layer 2 ($i = 2$). The real and imaginary parts of c_A and c_E in Eqn. (19) for this case are expressed as:

$$\text{Re}[c_A] = \left[E_1 \alpha_1 \frac{\delta_{k1}^3}{4k_1} f_-(\eta_1) - E_2 \alpha_2 \frac{\delta_{k2}^3}{4k_2} f_-(\eta_2) \right] B \tag{22}$$

$$\text{Im}[c_A] = \left[E_1 \alpha_1 \frac{\delta_{k1}^3}{4k_1} \left(\frac{2h_1}{\delta_{k1}} - f_+(\eta_1) \right) - E_2 \alpha_2 \frac{\delta_{k2}^3}{4k_2} \left(\frac{2h_2}{\delta_{k2}} - f_+(\eta_2) \right) \right] B \tag{23}$$

$$\text{Re}[c_E] = E_1 \alpha_1 \gamma_1 T_0 \left[\frac{1}{3} \left(h_0^3 + h_1^3 \right) + \frac{\delta_{k1}^3}{2} f_-(\eta_1) \right] + E_2 \alpha_2 \gamma_2 T_0 \left[\frac{1}{3} \left(h_2^3 - h_0^3 \right) + \frac{\delta_{k2}^3}{2} f_-(\eta_2) \right] \tag{24}$$

$$\text{Im}[c_E] = E_1 \alpha_1 \gamma_1 T_0 \frac{\delta_{k1}^3}{2} \left(\eta_1 - f_+(\eta_1) \right) + E_2 \alpha_2 \gamma_2 T_0 \frac{\delta_{k2}^3}{2} \left(\eta_2 - f_+(\eta_2) \right) \tag{25}$$

where

$$\eta_i = \frac{h}{2\delta_{k_i}} \tag{26}$$

$$f_+(z) = \frac{\sin(z) + \sinh(z)}{\cos(z) + \cosh(z)} \tag{27}$$

$$f_-(z) = \frac{\sin(z) - \sinh(z)}{\cos(z) + \cosh(z)} \tag{28}$$

where z is a dummy variable.

Case 2: Zero interfacial thermal resistance

Assuming that the thermal resistance at the interface is zero, heat is perfectly conducted and temperature is continuous at the interface, therefore:

$$k_2 \frac{\partial T_2}{\partial y} \bigg|_{y=h_0^+} = k_1 \frac{\partial T_1}{\partial y} \bigg|_{y=h_0^-} \tag{29}$$

$$T_2 |_{y=h_0^+} = T_1 |_{y=h_0^-} \tag{30}$$

By applying the counterpart of Eqs. (15), (16) and (30) in modal space, the coefficients C_i and S_i are found as:

$$[C_1, S_1, C_2, S_2]^T = M_c^{-1}(M_0 \hat{v} + M_2 \hat{v}_{xx}) \tag{31}$$

where the superscript T denotes matrix transpose and:

$$M_c = \begin{bmatrix} 0 & 0 & -\sin\left(\frac{\sqrt{-2i}}{\delta_{k2}} h_2\right) & \cos\left(\frac{\sqrt{-2i}}{\delta_{k2}} h_2\right) \\ \sin\left(\frac{\sqrt{-2i}}{\delta_{k1}} h_1\right) & \cos\left(\frac{\sqrt{-2i}}{\delta_{k1}} h_1\right) & 0 & 0 \\ \cos\left(\frac{\sqrt{-2i}}{\delta_{k1}} h_0\right) & \sin\left(\frac{\sqrt{-2i}}{\delta_{k1}} h_0\right) & -\cos\left(\frac{\sqrt{-2i}}{\delta_{k1}} h_0\right) & -\sin\left(\frac{\sqrt{-2i}}{\delta_{k1}} h_0\right) \\ -k_1 \frac{\sqrt{-2i}}{\delta_{k1}} \sin\left(\frac{\sqrt{-2i}}{\delta_{k1}} h_0\right) & k_1 \frac{\sqrt{-2i}}{\delta_{k1}} \cos\left(\frac{\sqrt{-2i}}{\delta_{k1}} h_0\right) & k_2 \frac{\sqrt{-2i}}{\delta_{k2}} \sin\left(\frac{\sqrt{-2i}}{\delta_{k2}} h_0\right) & -k_2 \frac{\sqrt{-2i}}{\delta_{k2}} \cos\left(\frac{\sqrt{-2i}}{\delta_{k2}} h_0\right) \end{bmatrix} \tag{32}$$

$$M_0^T = \left[\frac{\delta_{k2}}{\sqrt{-2i}} \frac{B}{k_2} \quad -\frac{\delta_{k1}}{\sqrt{-2i}} \frac{B}{k_1} \quad 0 \quad 0 \right]$$

$$M_2^T = \left[-\frac{-\delta_{k2}}{\sqrt{-2i}} \gamma_2 T_0 \quad -\frac{-\delta_{k1}}{\sqrt{-2i}} \gamma_1 T_0 \quad (\gamma_2 - \gamma_1) T_0 h_0 \quad (k_2 \gamma_2 - k_1 \gamma_1) T_0 \right]$$

Thus, c_A and c_E can be obtained by performing the integrals in Eqn. (14).

Once converted to modal space, the momentum equation (Eqn. (12)) is expressed as:

$$-\rho h \lambda^2 \hat{v} = \frac{\partial^2 \hat{m}}{\partial x^2} \tag{33}$$

Knowing c_A and c_E, Eqn. (33) becomes:

$$-\rho h \lambda^2 \hat{v} + (D + c_E) \frac{\partial^4 \hat{v}}{\partial x^4} + c_A \frac{\partial^2 \hat{v}}{\partial x^2} = 0 \tag{34}$$

A possible solution to the fourth order ODE in Eqn. (34) has the form $\hat{v} = e^{i\kappa_j x}$, where κ_j (with $j = 1, 2, 3, 4$) is the wavenumber obtained from the roots of the characteristic equation:

$$(D + c_E) \kappa^4 - c_A \kappa^2 - \rho h \lambda^2 = 0 \tag{35}$$

The complete solution of $\hat{v}$ to Eqn. (34) is:

$$\hat{v} = \sum_{j=1}^{4} C_j e^{i\kappa_j x} \tag{36}$$

The mode shape $\hat{v}$ satisfies cantilever beam boundary conditions:

$$\hat{v}(0) = 0 \tag{37}$$

$$\frac{\partial \hat{v}}{\partial x}(0) = 0 \tag{38}$$

$$\widehat{Q}(L) = -(D + c_E)\frac{\partial^3 \hat{v}}{\partial x^3}(L) - c_A \frac{\partial \hat{v}}{\partial x}(L) = 0 \tag{39}$$

$$\widehat{M}(L) = -(D + c_E)\frac{\partial^2 \hat{v}}{\partial x^2}(L) - c_A \hat{v}(L) = 0 \tag{40}$$

Substituting Eqn. (36) into the above boundary condition equations, they can be rewritten in a more compact form as:

$$\det[M_\kappa] = 0 \tag{41}$$

where the (i, j) th element in the 4x4 matrix M_κ is given by:

$$M_\kappa(1, j) = 1 \tag{42}$$

$$M_\kappa(2, j) = \kappa_j \tag{43}$$

$$M_\kappa(3, j) = \kappa_j \left[-(D + c_E)\kappa_j^2 + c_A \right] e^{i k_j L} \tag{44}$$

$$M_\kappa(4, j) = \left[-(D + c_E)\kappa_j^2 + c_A \right] e^{i k_j L} \tag{45}$$

Eq. (41) can then be solved for the complex frequency $\lambda = \omega - i\beta$.[1]

Numerical results

Consider a cantilever beam where layer 1 is made out of copper and layer 2 is made out of aluminum. The beam is subject to an inward heat flux $q = Bv$ applied at both the top and bottom surfaces. The relevant coefficients and parameters are listed in Table 1.

The application of the method described above yields the complex frequency λ for both Case 1 and Case 2. The corresponding results are 1) $\lambda_{c1w} = 6.6147 - 0.0868i$ [rad/s] and 2) $\lambda_{c2w} = 6.6104 - 0.0388i$[rad/s]. Note that the **c** in the subscripts indicates "**c**onstant h_0"; the **1** and **2** correspond to Case 1 and Case 2 respectively; and the **w** denotes "**w**ith TED". According to the $\lambda = \omega - i\beta$ notation, in both cases we get positive growth rates β, which indicates that the motion is being amplified exponentially. Remember that the structural damping, which counteracts the exponential growth, is not accounted for in this analyses. Damping ratio of metals is generally on the order of 10^{-3} [31].

The coefficient c_E can be viewed as a modification to the flexural rigidity due to the adiabatic thermoelastic coupling. The imaginary part of c_E, expressed as Eqn. (25), is positive regardless of the value of η_i, because the inequality $\eta - f_+(\eta) > 0$ always holds for $\eta > 0$. This result indicates that the modified flexural rigidity $(D + c_E)$ is complex with a small positive imaginary part, which leads to a slowly decaying response in time. This is the well-known thermoelastic damping effect, caused by *stress inhomogeneities* in the vibrating beam [29]. We can neglect the thermoelastic damping in order to evaluate its effect on the growth rate by setting $\gamma_i = 0$ in the energy equation (Eqn. (17)). The resulting eigenvalues λ for both cases are 1) $\lambda_{c1wo} = 6.6054 - 0.0871i$ [rad/s] and 2) $\lambda_{c2wo} = 6.6102 - 0.0396i$ [rad/s]. Note that the **wo** denotes "**w**ith**o**ut TED". Comparing these results with those obtained when keeping the thermoelastic coupling term in the energy equation, it is observed that β is slightly larger when the thermoelastic damping is neglected. Therefore it can be concluded that the thermoelastic coupling term in the energy equation has a small effect on the mechanical damping. In addition, if the heat flux (B) is large enough, the thermoelastic damping becomes negligible compared to the strong exponential growth caused by thermoacoustic instability.

The additional term associated with c_A accounts for the effects of the external heating by the coefficient B. Similar to the thermoelastic damping coefficient c_E, c_A is also complex, hence it is capable of inducing either a decaying or a growing response depending on the sign of Im[c_A]. A negative Im[c_A] produces motion amplification. It is seen by Eqn. (23) that the sign of Im[c_A] depends on the material properties of the two layers and on the sign of the coefficient B. To achieve a more intense thermoacoustic growth, a negative Im[c_A] with a larger absolute value is preferred. If the beam is thin compared to the thermal penetration thickness, that is $\eta_i \ll 1, f_+(\eta_i) \approx \eta_i$, hence Im[$c_A$] is approximately equal to:

---

[1] An alternative approach to find λ is to discretize Eqn. (34) in x and then solving the corresponding eigenvalue problem.

Table 1
Material properties and relevant parameters.

Layer 1		Layer 2	
$E_1 = 110[\text{GPa}]$	$\rho_1 = 8960 \ [\text{kg/m}^3]$	$E_2 = 70[\text{GPa}]$	$\rho_2 = 2700 \ [\text{kg/m}^3]$
$\alpha_1 = 17 \times 10^{-6}[\text{K}^{-1}]$	$k_1 = 400 \ [\text{W/(mK)}]$	$\alpha_2 = 23 \times 10^{-6}[\text{K}^{-1}]$	$k_2 = 238 \ [\text{W/(mK)}]$
$c_{\varepsilon_1} = 385 \ [\text{J/(kgK)}]$		$c_{\varepsilon_2} = 900 \ [\text{J/(kgK)}]$	
Dimensions		**Heating parameter**	
$h = 1/8[\text{inch}] = 3.175[\text{mm}]$	$L = 4.5[\text{ft}] = 1.37[\text{m}]$	$B = 10^6[(\text{W/m}^3)]$	

$$\text{Im}[c_A] \approx \left[E_1\alpha_1 \frac{\delta_{k1}^3}{4k_1}\left(\frac{2h_1}{\delta_{k1}} - \eta_1\right) - E_2\alpha_2 \frac{\delta_{k2}^3}{4k_2}\left(\frac{2h_2}{\delta_{k2}} - \eta_2\right)\right]B = \left[E_1\alpha_1\frac{\delta_{k1}^2}{4k_1}\left(\frac{h}{2} - 2h_0\right) - E_2\alpha_2\frac{\delta_{k2}^2}{4k_2}\left(\frac{h}{2} + 2h_0\right)\right]B$$

$$= \frac{\alpha_1}{2\omega(\rho_1 c_{\varepsilon_1})}\frac{E_1 E_2}{E_1 + E_2}h\left[1 - \left(\frac{\alpha_2}{\alpha_1}\right)\left(\frac{\rho_1 c_{\varepsilon_1}}{\rho_2 c_{\varepsilon_2}}\right)\right]B \tag{46}$$

Therefore, the following inequality is necessary to achieve flexural thermoacoustic instability:

$$H_1 \frac{E_1 E_2}{E_1 + E_2}\left[1 - \frac{H_2}{H_1}\right]B < 0 \tag{47}$$

where the ratio

$$H_i = \frac{\alpha_i}{(\rho_i c_{\varepsilon_i})} \tag{48}$$

is a measure of the rate of linear expansion of a thin material layer in response to a certain amount of heat being provided.

Eq. (47) shows that for conventional materials whose thermal and mechanical properties are positive ($H_i > 0$ and $E_i > 0$), the layer with higher ratio H should coincide with the hot region ($[1 - H_2/H_1]B < 0$), so that both the thermal bending and the phase lag between heating/cooling and deformation work together to amplify the motion. Further considerations for the interpretation of the mechanism at the basis of the instability associated with Eqn. (47) are provided in Section 4 and Fig. 6.

As depicted in Fig. 1(d) and (e), we consider the hot region being in the upper half plane ($B > 0$, i.e. $q > 0$ when $v > 0$), then the top layer (layer 2) requires larger thermal expansion coefficient α and lower heat capacity ρc_ε compared to the bottom layer. A lower heat capacity causes faster temperature changes when heated/cooled and a larger thermal expansion coefficient causes larger deformations induced by a given temperature fluctuation. A more detailed discussion on these aspects can be found in Section 4. Clearly, if the two layers are made out of the same material, $\text{Im}[c_A]$ becomes zero by Eqns. (22–23). Thus, a single layer beam being heated at the same rate on both sides cannot sustain thermoacoustically induced motion.

In summary, an asymmetric temperature distribution achieved via the use of an heterogeneous cross section can induce a non-zero thermal moment m_T capable of producing either a growing or a decaying response. This observation is consistent with the conclusions drawn in other studies on thermally induced vibrations [32,27,33,34].

By comparing the growth rate β of the two cases studied in previous sections, one can conclude that the heat transfer at the interface between the two layers is actually detrimental to the onset of the instability. This is due to the fact that the interfacial heat transfer tends to smear out some of the temperature asymmetry.

3.2. Time-varying neutral axis location (Varying h_0)

In this section, we remove the previous assumption of stationary neutral axis and we consider a more physically accurate condition where the location of the neutral axis can vary according to Eqn. (9). Note this case, also the flexural rigidity D is no longer a constant but it depends on x. The procedure to solve the equation is conceptually equivalent to that described in Section 3.1. Remembering that the thermoelastic damping effect is small when B is large (see first row of Table 2), we can neglect the thermoelastic coupling term by setting $\gamma_i = 0$ in order to simplify the analytical derivation.

The temperature fluctuation $\widehat{T}$ and the integral quantity $\hat{A}I_T$ are determined by Eqn. (17) with $\gamma_i = 0$. Since the heat flux $\hat{q}$ is proportional to $\hat{v}, \hat{A}I_T$ can be expressed as $\hat{A}I_T = c_T \hat{v}$. Thus:

$$h_0 = h_e - \frac{c_T}{h/2(n+1)}\frac{\hat{v}}{\hat{v}_{xx}} \tag{49}$$

By Eqn. (5), σ_i is a linear combination of $\hat{v}$ and $\hat{v}_{xx}$. From Eqn. (4):

$$m = \int_{-h_1}^{h_0} \sigma_1 y dy + \int_{h_0}^{h_2} \sigma_2 y dy = -\left(\phi_1 \hat{v} + \phi_2 \hat{v}_{xx} + \phi_3 \frac{\hat{v}^2}{\hat{v}_{xx}}\right) \tag{50}$$

Table 2

Values of λ calculated from Eqns. (34) and (51) with constant and varying h_0, respectively. Case 1 and 2 indicate bilayer beams having either infinite or zero interfacial thermal resistance, respectively. For the case of constant h_0, the eigenvalues λ calculated either with (w) or without (wo) thermoelastic damping (TED) are tabulated in the second row. Results show that the effect of TED is essentially negligible. The last row shows the eigenvalues λ for the case including both varying h_0 and negligible TED. These results are very close to those calculated from constant h_0.

λ	Case 1	Case 2
Constant h_0 w/. Eqn. (34)	$\lambda_{c1w} = 6.6147-0.0868i$ $\lambda_{c1wo} = 6.6054-0.0871i$	$\lambda_{c2w} = 6.6104-0.0388i$ $\lambda_{c2wo} = 6.6102-0.0396i$
Varying h_0 w/. Eqn. (51)	$\lambda_{v1wo} = 6.6053-0.0870i$	$\lambda_{v2wo} = 6.6100-0.0396i$

where ϕ_j (with $j = 1, 2, 3$) are constants determined by h_0 and the integral in Eqn. (50). Substituting Eqn. (50) into Eqn. (33) yields:

$$-\rho h\lambda^2 \hat{v} + \phi_1 \frac{\partial^2 \hat{v}}{\partial x^2} + \phi_2 \frac{\partial^4 \hat{v}}{\partial x^4} + \phi_3 \frac{\partial^2 (\hat{v}^2/\hat{v}_{xx})}{\partial x^2} = 0 \tag{51}$$

Since $h_0 = h_0(x)$ is x-dependent, Eqn. (51) is a nonlinear equation homogeneous in terms of $\hat{v}$ and its derivatives. This indicates that the mode shapes $\hat{v}$ in modal space are scale-independent, because linearity is sufficient but not necessary for homogeneity.

Eq. (51) can be discretized on x and solved by using a nonlinear algorithm for root extraction. The spatial derivatives are approximated by a second order central difference scheme. At each boundary, two ghost points are assumed, whose displacements are extrapolated according to a fourth order polynomial in order to ensure the boundary conditions. The eigenvalues λ and the mode shapes $\hat{v}$ are obtained for the same two cases considered in Section 3.1. The calculated values of λ for the two cases are 1) $\lambda_{v1wo} = 6.6053 - 0.0870i$ and 2) $\lambda_{v2wo} = 6.6100 - 0.0396i$, both are very close to the results in Section 3.1. The **v** in the subscripts denotes "**v**arying h_0" Table 2 summarizes the results calculated through Eqn. (34) and (51). Fig. 3 shows the mode shape $\hat{v}$, the neutral axis location h_0, and the effective flexural rigidity $D_{\text{eff}} = -\hat{m}/\hat{v}_{xx}$. The black solid lines in the mid and right columns in Fig. 3 indicate the reference values of the neutral axis location h_e and the flexural rigidity D_e for an elastic beam without thermoelastic coupling. Results show that both h_0 and D_{eff} resemble their elastic counterparts near the fixed end of the beam, while they deviate considerably near the free end. The imaginary part of D_{eff} being negative, similar to a negative $\text{Im}[c_A]$ described in Section 3.1, is another driver to achieve positive β, that is a growing motion.

From Fig. 3, note that although h_0 deviates considerably from h_e near the free end, the predicted eigenvalues are close to those of a constant h_0 (Table 2). Under the constant h_0 assumption, although the neutral axis location is assumed unaffected by the presence of heat, the thermal effect is captured by the thermal moment m_T in Eqn. (12). On the contrary, under the varying h_0 assumption the elastic and thermal moments become indistinguishable (Eqn. (51)), since the neutral axis location is coupled with the temperature field in the beam. Nonetheless, both assumptions return similar eigenvalues under same physical constraints.

Note that the eigenvalues and eigenfunctions (Table 2 and Fig. 3) analyzed in this section are associated with the first (fundamental) flexural mode of the beam because of the following reasons: (1) the fundamental mode has the lowest frequency, associated with larger amplitudes, translating into larger mechanical energy and power density, so it is the easiest to excite and more practical for real applications; and (2) both heating strategies adopted in this study provide uniform heat flux along beam axis, i.e. q independent of x. The fundamental mode of the beam takes full advantage of this axially-uniform heat profile because the flexural motion of each point on the beam, associated with the fundamental mode, is in phase. However, the higher modes have displacement nodes other than the clamped end, so the particles on both sides of the displacement node deflects out of phase. As a result, the heating and cooling effects, which are beneficial to the flexural instability for particles on one side of the displacement nodes, are detrimental to the instability for the particles on the other side. Therefore, to effectively trigger the flexural instability of higher modes, more complicated heating profiles would need to be designed considering the phase shift in the vicinity of the displacement node. For example, the heat flux needs to change sign when passing the displacement nodes in the axial direction.

4. Type II: $q = Q\text{sgn}(v)$ Heating

In this section, we consider a heating configuration which is more practical from an experimental standpoint. As depicted in Fig. 1, we consider a hot region in the upper half plane ($q = +Q$ when $v > 0$), and a cold region in the lower half plane ($q = -Q$ when $v < 0$). As soon as the geometrical center of the cross section is positively (negatively) displaced, the whole cross section experiences uniform surface heating (cooling) rate Q. This configuration, shown in Fig. 1(e), results in a non-harmonic heat flux so that the modal approach cannot be applied. Therefore, Eqn. (3) was solved by direct time integration with a forward-time-central-space (FTCS) scheme. The space was discretized in the same fashion as described in Section 3.2. A fourth order Runge-Kutta scheme with adaptive time step was adopted for the time integration. Note that according to Eqn. (9), h_0 might become singular in correspondence to a zero local curvature value, that is $v_{xx} = 0$. While this scenario
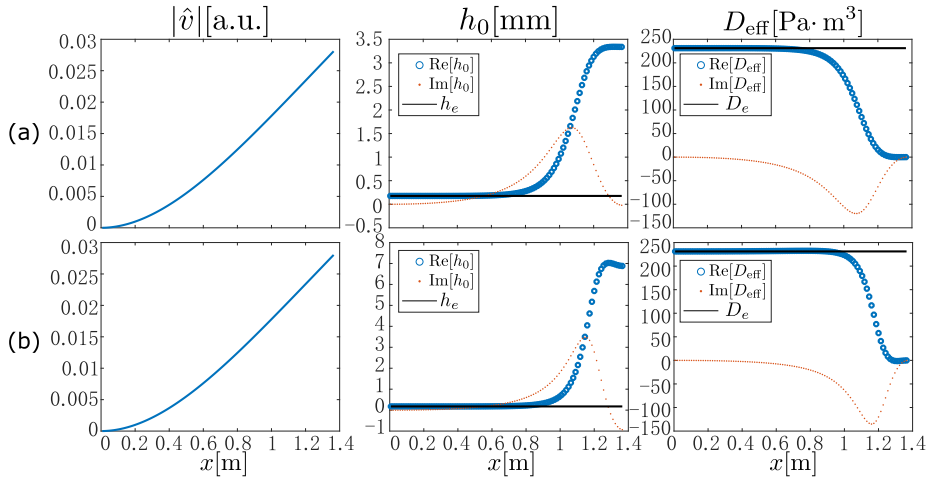
Fig. 3. Mode shape $|\hat{v}|$ (arbitrary units, abbreviated as a.u.), real (blue circles) and imaginary (orange dots) parts of neutral axis location h_0 and effective flexural rigidity D_{eff} for (a) Case 1. Infinite interfacial thermal resistance, and (b) Case 2. Zero interfacial thermal resistance. The black solid lines in h_0 and D_{eff} plots are the neutral axis location and flexural rigidity of a pure elastic beam as references.

is physically possible, as it indicates a local change of concavity, it is numerically challenging. Hence, in order to overcome this numerical issue, a continuous filter g is imposed on $(h_0 - h_e)/h$. The filter is given by:

$$g\left(\frac{h_0 - h_e}{h}\right) = \psi \tanh\left(\frac{1}{\psi}\frac{h_0 - h_e}{h}\right) \tag{52}$$

Note that $g(z) \approx z$ when z is small and $g(z) \approx \psi$ when z is large. z is a dummy variable. Fig. 4 shows the trend of this function for different values of the parameter ψ. In order to avoid the numerical instability in our study, we choose $\psi = 10000$ to approximate the case of zero curvature when h_0 approaches the singularity ($h_0 = \infty$). This filter preserves the local curvature's value (v_{xx}) when it is large, while it replaces it by a bounded value (associated with $(h_0 - h_e)/h = \psi$) when it is small ($v_{xx} \to 0$).

By solving Eqn. (3), we can evaluate the time evolution of h_0, v_{xx}, v, m and of the cross-sectional averaged thermal strain $\varepsilon_T = \alpha \langle T \rangle$ over each layer. In the latter expression, the angle brackets indicate layer-cross-sectional averaging (see also online supplementary material). Results show that 1) the motion of the beam is self-amplifying, and 2) a singularity in h_0 (i.e. a zero-curvature point) exists and propagates towards the fixed end. These two points are closely related to each other and are the result of two factors: 1) the existence of a phase lag between the thermal-induced deformation and the thermal perturbation, and 2) the differential expansion and contraction of each layer. The time evolution of ε_T (see supplementary video) shows that the thermal strain of the top layer increases (decreases) faster than the bottom layer when the beam is heated (cooled), thus insuring that the thermal strain of the top layer is larger (smaller) when the beam is moving downward (upward). This situation occurs because the top layer (here assumed to be aluminum) has a larger thermal expansion coefficient and a lower heat capacity so it reacts faster to the heat stimulus than the bottom one (here assumed to be copper). This observed behavior is consistent with the discussion on Eqn. (47) in Section 3.1.
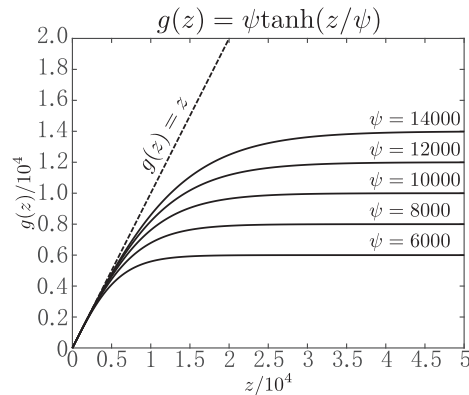

Fig. 4. The trend of the function $g(z)$ parameterized in ψ. The dashed line shows that $g(z) \approx z$ when z is small.
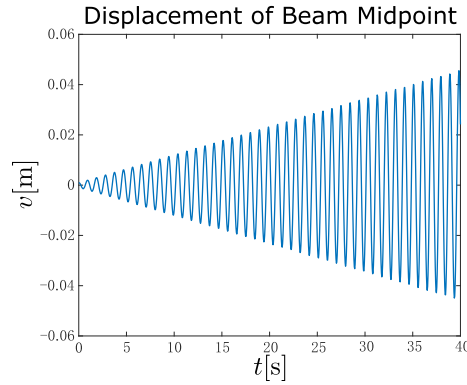
Fig. 5. Time history of the transverse displacement at the midpoint of the beam under $q = Q\text{sgn}(v)$ type heating.

Fig. 5 shows the time history of the transverse displacement of the beam's midpoint numerically calculated via time integration. Differently from the $q = Bv$ type heating, the motion grows linearly instead of exponentially. This is a clear evidence of a growing motion under spatial thermal gradient.

Figs. 6 (I-IV) show the four fundamental states occurring over each selected quarter of a period, that qualitatively explain the mechanism of flexural thermoacoustic response in the bilayer beam. In the first quarter of period (Fig. 6 (I)), the beam is warping upward while moving downward. The thermal strain ε_T of the top layer is larger than that of the bottom one, which makes the free end of the beam deflect downwards as a result of thermal bending. This effect changes the concavity of the beam, inducing a sign change of curvature and a singularity of h_0 at the same location. When the beam is in the upper half plane, the heating increases the difference between the elongation of the two layers, thus further increasing the bending of the beam downward. This mechanism explains why the singularity of h_0 propagates towards the fixed end (as visible in the supplementary material video). The downward thermal bending accelerates the downward elastic motion (compare the two rows in Fig. 6(I)), hence amplifying the motion. In the second quarter of period (Fig. 6 (II)), the beam is warping downward and moving downward as well. Although the beam is cooled since it is in the lower half plane, the temperature fluctuation, as well as ε_T, is still positive due to the phase delay with respect to heating. Therefore, there is still a thermally-induced downward bending which accelerates the original downward motion. However, in this quarter, the beam is elastically warping downward as well, so the additional thermally-induced downward bending does not change the sign of the curvature, but rather increases its absolute value. As a result, in this period, there is no singularity on h_0. The motion in the third and fourth quarters are analogous to the first and second, but the two layers contract instead of expanding.

An interesting observation can be drawn concerning the opportunities opened by SSTA devices. For all the configurations discussed above, the materials used for the two layers were assumed to have positive properties, i.e. $H_i > 0$ & $E_i > 0$, and satisfy Eqn. (47) by ensuring $[1 - H_2/H_1]B < 0$. In recent decades, the engineering community has made much progress in

Fig. 6. Conceptual schematic summarizing the flexural SSTA mechanism. In a given period of oscillation, the beam motion can be divided into four phases. (I, III) In the first (third) phase, the beam moves down (up), warps up (down) and is heated (cooled). The top layer expands (contracts) more than the bottom one does. Thus the beam under the effect of heat, bends down (up) starting from the free end, which (1) causes a sign change of the curvature, and (2) accelerates the downward (upward) motion. (II, IV) In the second (fourth) period, the beam moves and warps down (up), and is cooled (heated). In this phase, the temperature fluctuation, hence the thermal strain, is still positive (negative) due to the phase delay between temperature and heat flux. The top layer expands (contracts) more than the bottom one does. Thus, the beam under the effect of heat, bends down (up) further from the free end, which does not change the concavity along the beam but accelerates the downward (upward) motion. This schematic explains the self-amplifying mechanism of flexural SSTAs.

the discovery and development of engineered materials capable of unusual effective dynamic properties such as, for example, negative density [35], negative modulus [36], and negative thermal expansion coefficient (CTE) [37–39]. Assuming the availability of materials having such unusual properties, we could conceive a bilayer beam capable of satisfying $H_1 < 0$ or $E_1 E_2 / (E_1 + E_2) < 0$. For example, assuming the top layer still made of aluminum while replacing the bottom layer with a material exhibiting negative CTE (i.e. $\alpha_1 < 0$), Eqn. (47) could still be satisfied. With this combination of materials, the thermally-induced bending would be increased because the degree of thermal bending depends on the difference between the thermally-induced axial deformation of the two layers. Obviously, this difference increases if, during heating, one layer is expanded while the other is contracted. We merely note here that the use of a solid state medium as a basis for TA devices provides an excellent opportunity for tailoring the dynamic behavior and the resulting performance by leveraging engineered materials.

5. Experimental validation

In order to validate the concept of F-SSTAs as well as the corresponding modeling framework, we performed an experimental investigation. The experimental sample consisted in a bilayer beam made of a layer of Aluminum 6061 and a layer of Copper 110. The dimensions of each strip were 1/2 inch wide, 1/16 inch thick and 4.5 feet long (Fig. 7). The two metallic strips were combined in a bilayer beam by means of riveted joints spaced 2 inches along the axial direction (Fig. 7). Two rivets were used in the width direction. The beam was oriented in a vertical position, fixed at one end by a C-clamp, and with a 2 lbs mass attached to the free end by heat-resistant tape. The mass was applied in order to lower the fundamental frequency ω of the beam so to increase the time the beam is exposed to either heating or cooling. The fundamental frequency of the fixed-mass beam is approximately 0.5 Hz. Note that a larger thermal penetration depth $\delta_k \propto \sqrt{1/\omega}$ is in favor of the cross-sectional temperature variation subject to surface heating. The weight of the mass also limits the static thermal deformation of the beam which results from the differential expansion of the two layers. Two infrared (IR) lamps having a nominal power output of 1500 Watts were used as heat source. The lamps were located on the same side of the aluminum strip, for the argument following Eqn. (47). The dynamic response was measured via a Laser Doppler Vibrometer (LDV) at a point located 20 inches from the end mass.
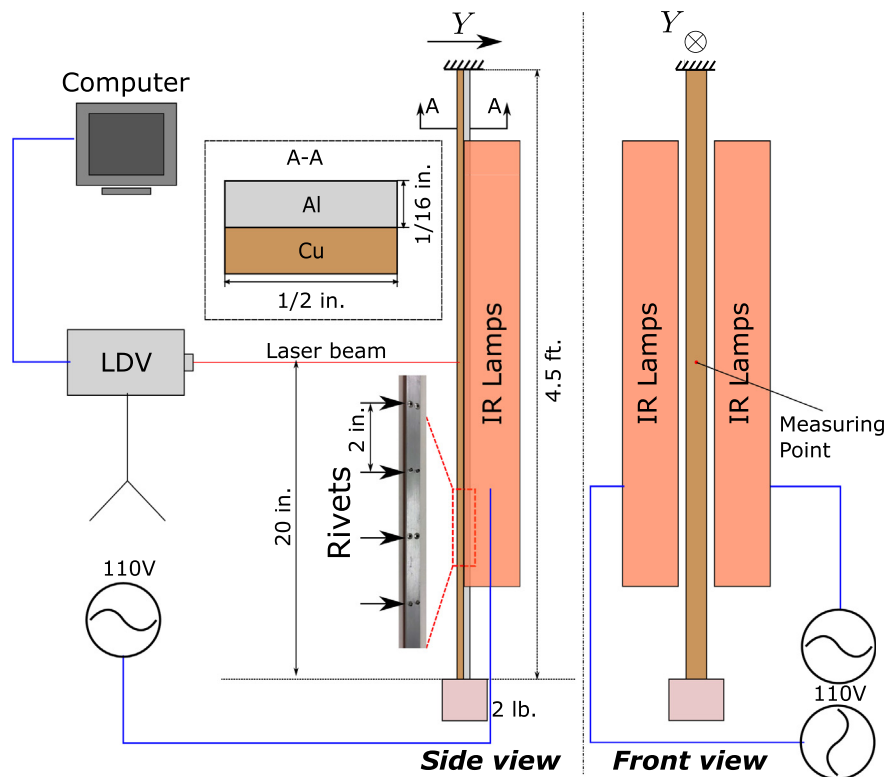

Fig. 7. A notional schematic of the experimental setup. The cantilever beam is made of one layer of Aluminum and one of Copper joined together by an array of rivets spaced 2 inches in the axial direction (inset photo). Two 1500 watts infrared (IR) lamps were used as heat source. A mass was applied at the free end to lower the fundamental resonance frequency of the beam and to counteract its static thermoelastic deformation. The response of the beam was measured in terms of the transverse displacement of the point located 20 inches from the free end. The dynamic response is measured by an LDV.

The perturbation needed to initiate the oscillatory response was provided by displacing the free end of the beam by approximately 10 inches. When the beam enters the heating region, it absorbs heat radiated by the IR lamps; when it leaves the heating region, it cools down by natural convection. Therefore, the combination of the heating region and the natural convection cooling form a spatial thermal gradient. Although less effective in creating strong thermal gradients, natural convection was preferred to forced convection because the latter might induce aerodynamic loading possibly alter the TA response of the beam.

A few considerations should be made comparing the experimental setup with the numerical model. The transition through the hot-cold region at the interface is not as sharp as considered in the numerical simulations. This is due to heat escaping the heating region through the opening realized to allow the oscillatory motion of the beam. Also, note that the heat source is fixed in space, so only when the equilibrium position of the beam is exactly aligned with the interface between the heating and the cooling regions, the physical thermal gradient would match the theoretical gradient of *Type II* thermal load. If equal amount of heating and cooling could be provided during one cycle, as assumed in the theory derived in Section 2, the equilibrium position of the beam would always coincide with the straight configuration. However, in practice, the cooling does not balance exactly the heat absorbed, hence producing an increase of the average temperature of the beam. The most direct result of this average temperature increase is a static deformation of the beam due to the differential thermal expansion of the two layers. The end mass partially helps counteracting this static thermal deformation.

The experimental data were acquired under three different conditions: (1) lamps off, (2) lamps on with the beam moving only within the hot region, and (3) lamps on with the beam moving across the thermal gradient. Condition (1) captures the response of the beam at room temperature and in presence of structural damping. Condition (2) corresponds to the oscillatory motion of the beam occurring always in a hot environment, which leads to stronger thermoelastic damping effect. The decay in this case should be larger than Condition (1). Recall that, as discussed in Sections 3 and 4, the decay induced by thermoelastic damping is negligible compared to the large growth due to strong F-SSTA effect. However, in Condition (2), the F-SSTA effect is absent, so the thermoelastic effect must be noticeable. Condition (3) correspond to the beam operating under actual F-SSTA conditions. Note that here we use the term **Condition** to refer to different experimental arrangements, distinct from the term **Case** in Section 3, which was used for different interfacial thermal resistances.

Fig. 8 (a) presents the envelope of the measured transverse displacement history in these three conditions. Five measurements for each condition were taken. The solid lines displayed in Fig. 8 show the algebraic mean of these five data sets. The shaded area represents the 3σ standard deviations from the mean. The expected decay of the oscillatory motion due to either the structural or the thermoelastic dissipative mechanisms can be observed in Conditions (1) and (2). The response in Condition (2) decays faster because both dissipative mechanisms (i.e. structural and thermoelastic) are active. In Condition (3), that is the F-SSTA condition, a self-sustaining motion could not be observed due to an insufficient thermal gradient. A few aspect contributed to this low grade thermal gradient: (1) the low directivity of the IR lamps which disperse part of the heat away from the beam; (2) the cooling capacity of natural convection is limited; (3) part of the heat from the hot region leaks into the cold region via the opening left for the motion of the beam, hence decreasing the strength of the thermal gradient (compared to numerical case). Nonetheless, this data set still provides useful information to characterize the dynamics of the system. By visual comparison, it appears that in Condition (3) the amplitude of the displacement is the largest and the decay rate is the lowest. More quantitatively, the displacement level in Condition (3) is 13.5 dB and 25.2 dB higher than that of
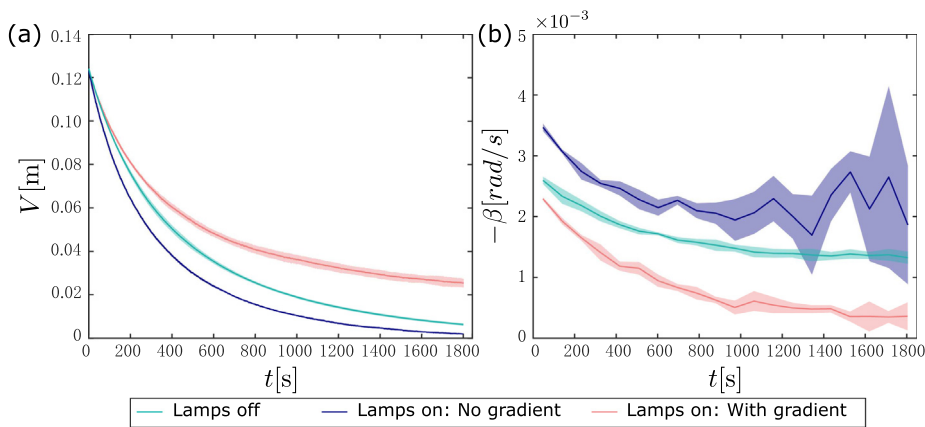

Fig. 8. (a) Envelope of the measured displacement (frequency ≈ 0.5 Hz) for the three heating conditions. Condition (1), "Lamps off" shows that the damping ratio of the bilayer beam is $\sim 1.3 \times 10^{-3}$, consistent with observed values typical of metals. Condition (2), "Lamps on: No gradient" decays the fastest due to the additional thermoelastic damping at high temperature. Condition (3), "Lamps on: With gradient" corresponds to the F-SSTA conditions. Although no self-sustained oscillations could be observed in this condition, an evident and strong reduction of the decay rate highlights the amplifying effect of the TA response. (b) Calculated decay rates (i.e. the inverse of the growth rate β) with time. The large deviations from the mean value observed towards the end of the time window in the condition "Lamps on: No gradient" are due to the signal decaying quickly below the noise floor level. Solid lines: mean value of five measurements in each condition. Shaded region: 3σ error deviation from the mean.

Condition (1) and Condition (2), respectively. The decay rate (Fig. 8 (b)) is calculated by using a logarithmic decrement approach combined with a sliding window having length of 93 s ($\sim$ 20 cycles). In all conditions, the decay rate is large during the initial part of the transient, while it decreases as the amplitude of the oscillation reduces. This trend can be explained as losses due to both structural and aerodynamic damping are directly related to the amplitude of the transverse displacement. Other effects affecting the global decay rate can include friction forces at the riveted interface between the two layers. As the motion reaches lower amplitudes, the decay rate stabilizes around a constant value. The decay rates of the three conditions are extracted and compared in this range. In Condition (1), the decay rate induced by structural damping is around 1.3×10^{-3}, which is consistent with the average value of the damping ratio for metals [31]. The higher dissipation in Condition (2), due to the additional thermoelastic damping, induces a fast decay of the response that falls quickly below the noise floor level. Therefore, the measured signal is actually dominated by the ambient noise which explains the larger fluctuations towards the end of the time window. In Condition (3), the decay rate nearly reaches zero towards the end of the time window, hence showing an evident delay of damping under the effect of the spatial thermal gradient. This reduction in decay rate (or, equivalently, enhancement in growth rate) is due to the thermo-mechanical energy conversion occurring in the F-SSTA process. By subtracting the time signal in Condition (1) from that in Condition (3), the amplified motion induced by the thermoacoustic instability can be obtained. In summary, even if a self-sustained thermoacoustic response could not be obtained in the current setup, the hallmarks of thermoacoustic growth are clearly present in the experimental data. It is expected that the use of a more powerful and concentrated heat source, as well as of a more effective cooling mechanism, could help significantly the formation of a stronger thermal gradient, thus facilitating the onset of self-sustained flexural vibrations.

6. Comparison between F-SSTA and thermal flutter

In this section, we present a conceptual comparison between the concept of F-SSTA presented in this study and the concept of thermal flutter that was explored in the late 1960s [28]. The thermal flutter phenomenon was discovered in the study of the dynamic thermoelastic response of boom-like structures operating in outer space environment. In thermal flutter, one side of a thin-walled boom with open annular cross section was subject to direct radiation from sunlight, while the other side remained in the dark hence radiating heat to deep space. Under these conditions, the boom exhibited either torsional or flexural instability depending on the specific design of the boom's cross section. By revisiting Eqn. (3), we observe that in both configurations a non-zero thermal moment gradient ($\partial^2 m_T / \partial x^2$) is necessary to achieve a heat-induced flexural instability. This condition further requires $m_T(x) \neq 0$ and $\partial m_T(x) / \partial x \neq 0$. The differences between F-SSTAs and the thermal flutter are mainly reflected in how these two conditions are satisfied.

In the flexural thermal flutter configuration, two main causes contribute to the occurrence of the instability: (1) the existence of a local thermal moment due to an asymmetric temperature distribution across the cross section of the beam which results from a single side exposure to the heat source ($m_T(x) \neq 0$); (2) as the beam bends, the non-uniform distance from the heat source of points located along the beam longitudinal axis leads to a non-uniform heat absorption, creating a non-zero thermal moment gradient along the beam ($\partial m_T(x) / \partial x \neq 0$). The thermal moment gradient effectively contributes to a thermal-induced motion.

In the context of F-SSTA, both sides of the beam experience identical heating (cooling), but the local thermal moment is achieved by utilizing two layers of distinct materials. Different thermal properties of both layers give rise to asymmetric temperature distribution over the cross section, while the difference in thermal expansion coefficients contribute to a distinct thermal strain. The combination of both these effects leads to a non-zero local bending moment ($m_T(x) \neq 0$). The thermal moment gradient ($\partial m_T(x) / \partial x \neq 0$) is formed by the spatially-varying and dynamically-changing neutral axis location h_0, under the effect of the localized thermal gradient.

Despite both phenomena rely on a non-uniform thermal moment distribution, we emphasize the necessity of a spatial thermal gradient in the F-SSTA configuration which is the foundation of the thermoacoustic instability.

7. Conclusion

In this paper, we extended the science of thermoacoustics to include self-sustained instabilities of flexural waves (F-SSTAs); a unique response modality typical of solid media. The mathematical framework of F-SSTAs was established and used to analyze the instability of the transverse bending motion in a bilayer slender beam. By employing a simplified heating strategy, both an analytical modal solution and a criterion to determine the onset of the flexural instability were obtained. According to this criterion, in natural materials, the layer with higher ratio of thermal expansion coefficient to heat capacity should be placed on the side where heat is provided (i.e. the hot region). However, for engineered materials in which unconventional properties can be achieved (e.g. negative modulus or negative thermal expansion coefficient) extreme thermoacoustic performance could be anticipated. This is a unique opportunity opened by solid-state thermoacoustics and could be particularly relevant for device applications. Numerical simulations in both the frequency and time domains helped revealing the mechanism of motion amplification due to flexural instability. More specifically, the time dependence of the location of the neutral axis under thermoacoustic coupling was observed and found to be a key aspect in the development of the instability. An experimental setup was also developed in order to validate the theoretical framework of F-SSTAs.

Although no evident self-sustained motion was observed, due to the limited heating and cooling capacity, the ultra-low effective damping was found to be a confirmation of the thermal-to-mechanical energy conversion due to the F-SSTA process.

Compared to its axial counterpart, flexural thermoacoustic vibrations are easier to excite in slender structures, and are associated with lower fundamental frequencies and larger amplitude of the response. All these aspects can result in significantly easier implementation and higher power density, both aspects of key relevance for the fabrication of thermoacoustic devices.

CRediT authorship contribution statement

Haitian Hao: Conceptualization, Formal analysis, Investigation, Methodology, Software, Validation, Visualization, Writing - original draft. **Carlo Scalo:** Conceptualization, Funding acquisition, Supervision, Methodology, Writing - review & editing. **Fabio Semperlotti:** Conceptualization, Funding acquisition, Project administration, Resources, Supervision, Writing - review & editing.

Declaration of Competing Interest

The authors declare that they have no known competing financial interests or personal relationships that could have appeared to influence the work reported in this paper.

References

[1] N. Rott, Damped and thermally driven acoustic oscillations in wide and narrow tubes, Z. Angew. Math. Phys. 20 (2) (1969) 230–243, https://doi.org/10.1007/BF01595562.
[2] J.L. Rayleigh, The explanation of certain acoustical phenomena, Nature 18 (1878) 319–321, https://doi.org/10.1038/018319a0.
[3] G. Swift, Thermoacoustic engines, J Acoust Soc Am. 84 (4) (1998) 1145–1180, https://doi.org/10.1121/1.396617.
[4] T. Yazaki, A. Iwata, T. Maekawa, A. Tominaga, Traveling wave thermoacoustic engine in a looped tube, Phys. Rev. Lett. 81 (15) (1998) 3128–3131, https://doi.org/10.1103/PhysRevLett.81.3128.
[5] C.J. Lawn, G. Penelet, Common features in the thermoacoustics of flames and engines, Int. J. Spray Combust. Dyn. 10 (1) (2018) 3–37, URLhttps://doi.org/10.1177/1756827717743911.
[6] J. Tan, J. Luo, Y. Wang, J. Wei, T. Jin, Performance of an air-cooled looped thermoacoustic engine capable of recovering low-grade thermal energy, Int. J. Energy Res. 44 (4) (2020) 2682–2692, https://doi.org/10.1002/er.5034.
[7] S.L. Garrett, D.F. Gaitan, D.K. Perkins, D.A. Helseth, Thermoacoustic life sciences refrigerator, J. Acous. Soc. Am. 93 (4) (1993) 2364, https://doi.org/10.1121/1.406185.
[8] J. Xu, E. Luo, S. Hochgreb, Study on a heat-driven thermoacoustic refrigerator for low-grade heat recovery, Appl. Energy 271 (2020), https://doi.org/10.1016/j.apenergy.2020.115167 115167.
[9] P. Rijke, LXXI. Notice of a new method of causing a vibration of the air contained in a tube open at both ends, Philos Mag Ser. 17 (116) (1859) 419–422, https://doi.org/10.1080/14786445908642701.
[10] K. De Blok, Low operating temperature integral thermo acoustic devices for solar cooling and waste heat recovery, J. Acoust. Soc. Am. 123 (5) (2008) 3541, https://doi.org/10.1121/1.2934526, 3541.
[11] T. Jin, R. Yang, Y. Wang, Y. Liu, Y. Feng, Phase adjustment analysis and performance of a looped thermoacoustic prime mover with compliance/resistance tube, Appl. Energy 183 (2016) 290–298, https://doi.org/10.1016/j.apenergy.2016.08.182.
[12] J. Tan, J. Wei, T. Jin, Onset and damping characteristics of a closed two-phase thermoacoustic engine, Appl. Therm. Eng. 160 (2019), https://doi.org/10.1016/j.applthermaleng.2019.114086 114086.
[13] J. Tan, J. Wei, T. Jin, Electrical-analogy network model of a modified two-phase thermofluidic oscillator with regenerator for low-grade heat recovery, Appl. Energy 262 (2020), https://doi.org/10.1016/j.apenergy.2020.114539 114539.
[14] M.T. Migliorino, C. Scalo, Real-fluid effects on standing-wave thermoacoustic instability, J. Fluid Mech. 883 (2020) A23, https://doi.org/10.1017/jfm.2019.856.
[15] C. Scalo, S. Lele, L. Hesselink, Linear and nonlinear modelling of a theoretical travelling-wave thermoacoustic heat engine, J Fluid Mech. 766 (2015) 368–404, https://doi.org/10.1017/jfm.2014.745.
[16] J. Lin, C. Scalo, L. Hesselink, High-fidelity simulation of a standing-wave thermoacoustic-piezoelectric engine, J. Fluid Mech. 808 (2016) 19–60, https://doi.org/10.1017/jfm.2016.609.
[17] P. Gupta, G. Lodato, C. Scalo, Spectral energy cascade in thermoacoustic shock waves, J. Fluid Mech. 831 (2017) 358–393, https://doi.org/10.1017/jfm.2017.635.
[18] G. Chen, L. Tang, B.R. Mace, Bistability and triggering in a thermoacoustic engine: A numerical study, Int. J. Heat Mass Transfer 157 (2020), https://doi.org/10.1016/j.ijheatmasstransfer.2020.119951 119951.
[19] Z. Yu, A.J. Jaworski, S. Backhaus, Travelling-wave thermoacoustic electricity generator using an ultra-compliant alternator for utilization of low-grade thermal energy, Appl. Energy 99 (2012) 135–145, https://doi.org/10.1016/j.apenergy.2012.04.046.
[20] K. Wang, D. Sun, J. Zhang, Y. Xu, K. Luo, N. Zhang, J. Zou, L. Qiu, An acoustically matched traveling-wave thermoacoustic generator achieving 750 w electric power, Energy 103 (2016) 313–321, https://doi.org/10.1016/j.energy.2016.03.001.
[21] G. Chen, L. Tang, B.R. Mace, Modelling and analysis of a thermoacoustic-piezoelectric energy harvester, Appl. Therm. Eng. 150 (2019) 532–544, https://doi.org/10.1016/j.applthermaleng.2019.01.025.
[22] G. Chen, L. Tang, Z. Yang, K. Tao, Z. Yu, An electret-based thermoacoustic-electrostatic power generator, International Journal of Energy Research n/a (n/a). URLhttps://onlinelibrary.wiley.com/doi/abs/10.1002/er.5019..
[23] H. Hao, C. Scalo, M. Sen, F. Semperlotti, Thermoacoustics of solids: a pathway to solid state engines and refrigerators, J Appl Phys. 123 (2) (2018), https://doi.org/10.1063/1.5006489 024903.
[24] H. Hao, C. Scalo, M. Sen, F. Semperlotti, Solid-state thermoacoustics, in: INTER-NOISE 2018–47th International Congress and Exposition on Noise Control Engineering: Impact of Noise Control Engineering, Vol. 258, 2018, pp. 432–439..
[25] H. Hao, C. Scalo, F. Semperlotti, Traveling and standing thermoacoustic waves in solid media, J Sound Vib. 449 (2019) 30–42, https://doi.org/10.1016/j.jsv.2019.02.029.
[26] H. Hao, C. Scalo, F. Semperlotti, Axial-mode solid-state thermoacoustic instability: an analytical parametric study, J. Sound Vib. 470 (2020), https://doi.org/10.1016/j.jsv.2019.115159 115159.

[27] F. Rimrott, R. Abdel-Sayed, Flexural thermal flutter under laboratory conditions, T Can Soc, Mech Eng 4 (4) (1976) 189–196, https://doi.org/10.1139/tcsme-1976-0027.

[28] R.M. Beam, On the phenomenon of thermoelastic instability (thermal flutter) of booms with open cross section, NASA TN-D5222. URL: https://ntrs.nasa.gov/archive/nasa/casi.ntrs.nasa.gov/19690020211.pdf..

[29] C. Zener, Internal friction in solids II. General theory of thermoelastic internal friction, Phys. Rev. 53 (1938) 90–99, https://doi.org/10.1103/PhysRev.53.90.

[30] M.A. Biot, Thermoelasticity and irreversible thermodynamics, J Appl Phys 27 (3) (1956) 240–253, https://doi.org/10.1063/1.1722351.

[31] J. Zhang, R. Perez, E. Lavernia, Documentation of damping capacity of metallic, ceramic and metal-matrix composite materials, J. Mat. Sci. 28 (1993) 2395–2404, https://doi.org/10.1007/BF01151671.

[32] B.A. Boley, Thermally induced vibration of beams, J. Aeronaut. Sci. 23 (2) (1956) 179–181.

[33] N.D. Jadeja, T.-C. Loo, Heat induced vibration of a rectangular plate, J. Eng. Ind. 96 (3) (1974) 1015–1021, https://doi.org/10.1115/1.3438401.

[34] G. Manolis, D. Beskos, Thermally induced vibrations of beam structures, Comput Method Appl M 21 (3) (1980) 337–355, https://doi.org/10.1016/0045-7825(80)90101-2.

[35] H.H. Huang, C.T. Sun, G.L. Huang, On the negative effective mass density in acoustic metamaterials, Int J Eng Sci. 47 (4) (2009) 610–617, https://doi.org/10.1016/j.ijengsci.2008.12.007.

[36] R.S. Lakes, T. Lee, A. Bersie, Y.C. Wang, Extreme damping in composite materials with negative-stiffness inclusions, Nature 410 (6828) (2001) 565–567, https://doi.org/10.1038/35069035.

[37] R. Lakes, Cellular solid structures with unbounded thermal expansion, J. Mater. Sci. Lett. 15 (6) (1996) 475–477, https://doi.org/10.1007/BF00275406.

[38] R. Lakes, Cellular solids with tunable positive or negative thermal expansion of unbounded magnitude, Appl Phys Lett. 90 (22) (2007), https://doi.org/10.1063/1.2743951 221905.

[39] H. Xu, D. Pasini, Structurally efficient three-dimensional metamaterials with controllable thermal expansion, Sci Rep. 6 (1). URLhttps://doi.org/10.1038/srep34924..